ADVANCED FUNCTIONAL MATERIALS
www.afm-journal.de

Materials Views
www.MaterialsViews.com

Directed Electric Field *Z*-Alignment Kinetics of Anisotropic Nanoparticles for Enhanced Ionic Conductivity

*Saurabh Batra, Emre Unsal, and Miko Cakmak**

In this study, the fast transient evolution of the electric field assisted thickness *Z*-direction orientation and assembly of clay particles is studied using a instrumented real time system that simultaneously measures in-plane and out of plane birefringence. The optical anisotropy master curves are developed, connecting the exposure time and electric field strength with orientation, using a superposition principle. *Z*-oriented nanocomposite films manufactured through the R2R process show enhancement through thickness ionic conductivity, useful for membranes of batteries and fuel cells.

1. Introduction

The addition of nanoparticles in polymeric systems offers potential for new and unique material properties at low particle concentrations.[1–4] This field has been heavily explored for mechanical[5–7] and diffusion property[8,9] enhancements with limited success. Many of these nanoparticles exhibit high anisotropy in their properties of interest including thermal conductivity,[10] diffusivity,[11] capacitance,[12] optical,[13] compressive strength,[14] and so on. However, traditional processing methods do not take advantage of these anisotropies as they are unable to orient the particles in the thickness direction.[15,16] In many applications like flexible electronics,[17,18] membranes,[19] supercapacitors,[20,21] fuel cells,[22] photovoltaics,[23] and so forth, the property of interest to enhance is in the thickness *Z*-direction. This is possible by utilizing directed field assisted assembly techniques such as electric field.[24–27] In this paper, we describe a comprehensive study of *Z*-direction alignment kinetics of clays in electric field and demonstrate the manufacture of large continuous films using a newly developed continuous roll-to-roll process that applies electric field for clay orientation followed by UV curing to rapidly freeze-in the obtained structure.

Layered clay platelets with their high aspect ratio enhance gas barrier properties in nanocomposites,[28] particularly when they are oriented with their broad surfaces in the plane normal to the diffusion direction. This orientation is easy to achieve by traditional flow processes such as extrusion,[29–31] film blowing,[32] and film stretching including uniaxial[33] and biaxial[34] stretching.

Clay nanocomposites can also be used for other properties including thermal conductivity,[35] ionic conductivity,[36] dielectric properties,[37,38] optical properties,[39] and so on,[40] if they are organized and oriented in the thickness direction. The traditional processes involving flow are not adequate for this alignment and thus externally induced directed self-assembly techniques utilizing electrical, magnetic or thermal fields may be used. To achieve directed orientation, a great deal of research has been devoted to electric field assisted alignment to create spatially and directionally oriented anisotropic nanocomposites in the past decade.[41–43] In electric field, a particle experiences torque from its permanent dipole (charged particles) or induced dipole (dielectric particles) movement. This induces both rotational and translational motion of particles in the matrix that leads to orientation as well as chaining of particles.[44–47] The anisotropy created by motion of the particles in electric field leads to changes in optical parameters including birefringence, IR dichroism, light transmission and scattering due to the intrinsic anisotropy in many of the nanoparticles[48,49]

In situ electric field induced orientation of suspensions of clay platelets has been studied using online small angle X-ray scattering (SAXS)[50] and wide angle X-ray scattering (WAXS)[51,52] techniques. However, these are generally not fast enough to follow rapid changes that could take place during alignment. In addition, WAXS technique relies on the diffraction signal coming from the still intact tactoids to represent the total clay filled system excluding fully exfoliated particles from their analysis. Birefringence is a powerful technique to determine the orientation of anisotropic particles because of their varying refractive index in the in-plane and out-of-plane direction, hence representing ensemble average contributions from exfoliated as well as multilayered clay tactoids. Orientation studies of clay platelets through electric birefringence have been limited to colloidal[53,54] and charged solutions[55] with low concentration (<0.5 wt%) of particles. In addition, these studies have been limited to batch processing; however for their wider utility, they need to be processed continuously.

The present study is divided into two parts: the first part focuses on the real time measurement system to determine the kinetics of clay orientation under the applied field with a highly instrumented integrated measurement system.[56] The second part involves roll-to-roll continuous photocurable monomer casting based processing utilizing optimized process variables obtained in the first part,[57] to create indefinitely long directionally anisotropic films where clay platelets are aligned through the thickness (Z-direction) of the film. The liquid casting based method was chosen for this application since particles are

Dr. S. Batra, Dr. E. Unsal, Prof. M. Cakmak
Department of Polymer Engineering
The University of Akron
Akron, OH 44325, USA
E-mail: cakmak@uakron.edu

DOI: 10.1002/adfm.201400760

easier to disperse at lower viscosities of monomer as compared to melt systems. In monomer dispersed particles, the lower drag forces increase the efficacy for rotational and translational motion of particles under electric field, thus increasing the orientation of aligned nanocomposite film. To control various processing parameters and conditions along with optical properties, the optical anisotropy was measured using a real time birefringence measurement system which helped determine the kinetics of rotation of anisotropic nanoparticles and development of orientation during electric field alignment. Further using the kinetics measurements, a master curve was developed with the electric-optic superposition (EOSP) principle which acts as a useful tool in building a structure property relationship to tailor various properties of nanocomposites along with processing parameters required for roll-to-roll manufacturing of oriented films.

2. Results and Discussion

2.1. Real Time Electric-Birefringence Measurement

We recently developed a real time measurement system for tracking fast temporal changes in birefringence, weight, thickness and surface temperature during drying of solution cast films (**Figure 1**a). Details of the instrument and its measurement capabilities on various polymeric systems can be found elsewhere.[56,58–60] For this study, its design was enhanced to measure the changes in both in-plane and out-of-plane birefringence during electric field application. It uses two indium tin oxide (ITO) coated glasses on top of each other separated by a glass spacer which is placed in the light path (Figure 1b) of the optical system described below. Different voltages with varying frequencies were applied through the ITO coated glasses and resulting fast temporal changes in the birefringence were recorded.

The optical system that measures the birefringence consists of two light sources with wavelengths in the visible range, linear polarizers, fiber optic cables and visible spectrometers (Avantes, Avaspec-NIR256–2.5). One linearly polarized light beam passes normal (parallel to the electric field vector) to measure in plane retardation (thus birefringence). The second linearly polarized light beam passes through the film at 45° to the film normal and electric field vector oriented to measure the out of plane retardation (and birefringence). The data was collected by four channel spectrometers and real time calculations at 10 data/s were carried out with custom designed software. Detailed procedures were discussed in our previous publication.[61]

The in-plane birefringence can then be calculated by dividing the retardation measured at 0° (R_0) by thickness (d_{eff}: effective thickness contributing to retardation development) as shown in Equation 1. Out-of-plane birefringence was calculated using Equation 2[62] where d_{eff} is the thickness, R_0 is the measured 0° retardation, $R\theta$ is the retardation value measured at θ degrees (where $\theta = 45°$ in our system) and $\bar{n}$ is average refractive index of the material. Though the system measures the full dispersion curve from 350–700 nm, only the optical properties corresponding to 546 nm is reported.

$$\Delta n_{12} = \frac{R_0}{d_{\text{eff}}} \tag{1}$$

$$\Delta n_{23} = \frac{1}{d_{\text{eff}}}\left[\frac{R_0 - R_\theta\left(1-\frac{\sin^2\theta}{\bar{n}^2}\right)^{1/2}}{\frac{\sin^2\theta}{\bar{n}^2}}\right] \tag{2}$$

The optical components in the system were set up to get a positive in-plane retardation when higher refractive index is in the long axis of the machine (Figure 1a) whereas negative in-plane retardation values indicate higher refractive index is in the transverse to the long axis of the machine. Similarly, a positive out-of-plane retardation is observed for higher refractive index in the film plane whereas a negative out-of-plane retardation implies higher refractive index is in the thickness direction of the film.

When electric field is applied to a dielectric matrix containing inorganic particles, these particles undergo induced polarization, the extent of which depends on the field variables (AC or DC). The field gradients experienced by these polarized particles lead to rotational and translational motion within the matrix.[63] Using the setup described above, the rapidly occurring rotational motion and preferential orientation direction of the intrinsically optically anisotropic particles can be tracked.

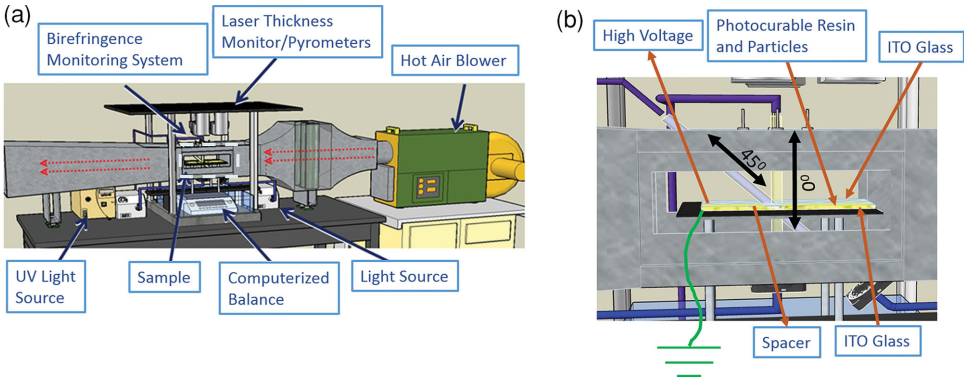

Figure 1. a) Real time solution drying platform which measures changes in out-of-plane and in-plane retardation along with thickness, weight and temperature measurements, b) modified setup to measure electric birefringence in both in-plane and out-of plane direction.

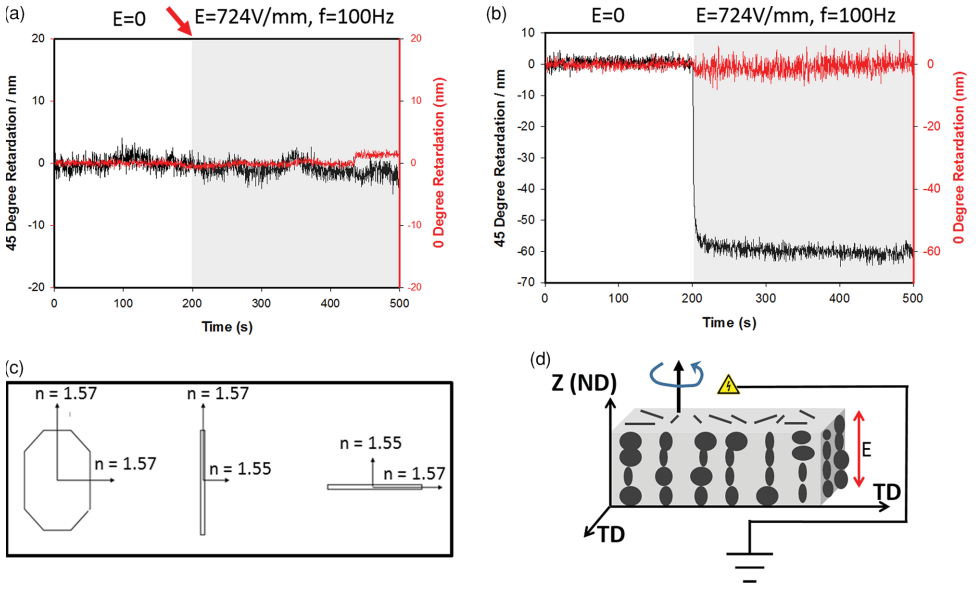

Figure 2. Response of in-plane and out-of-plane retardation on application of electric field on a) pure resin and b) 6 wt% clay filled system with applied field of 724 V/mm at 100 Hz; c) schematic showing in-plane and out-of plane refractive index of clay platelet and d) schematic of the of clay platelets aligned in polymer films. Arrows indicate the start of the e-field.

As the clay platelets (Cloisite 30B) in monomer (NOA65) were subjected to an AC (100Hz) electric field through the thickness direction (**Figure 2**b), the in-plane retardation remained at zero value, however, the out of plane retardation rapidly decreased to a negative value. To verify if this response was only due to clay orientation and there was no contribution of monomer on retardation, the same test was repeated (Figure 2a) without any filler and no appreciable change in both in-plane and out-of-plane retardation was observed with applied electric field. Since the retardation changes were only observed in the presence of clay platelets, the effective thickness of clay platelets in the polymer film was used to calculate the corresponding in-plane and out-of-plane birefringence changes using Equation 1,2. The average refractive index of the clay filled monomers was measured using Abbe Refractometer, Table S1 (Supporting Information) shows the refractive indices at different clay concentrations.

As mentioned earlier, the montmorillonite based clays are optically anisotropic.[33] They exhibit the same refractive index, 1.57, in all directions within the basal plane (001). Normal to the basal plane, the refractive index is 1.55 making the intrinsic birefringence $\Delta n^{\circ}_{clay} = n^{\circ}_{\perp} - n^{\circ}\| = -0.02$ (Figure 2c). This showed that the (001) planes orient along the thickness or the electric field direction when the field is turned on. Simultaneously, we observed zero in-plane retardation as these particles exhibit rotational randomness in the through–view direction as the $n^{\circ}_{\perp}$ and $n^{\circ}\|$ values statistically average leading to zero in plane retardation and thus birefringence (Figure 2d).

2.2. Kinetics and Orientation of Alignment

Colloidal particles suspended in aqueous medium, liquid crystals and other dilute systems have complex frequency dependence on electric field polarizability. The effect of frequency depends on the composition, shape, size, electric double layer and conductivity of the solvent. A series of tests at constant voltage and particle concentration with varying frequency from DC to 1 kHz (system limitation) was carried out for clay platelets in photocurable monomer system. However, in contrast to the colloidal particles and liquid crystal systems, no frequency dependence in the maximum orientation or rate of change of orientation was observed in our system (Figure S1, Supporting Information). Similar observations have been previously seen for clays in viscous solutions.[50]

To study the orientation kinetics, birefringence studies were carried out at varying concentrations and applied voltages. A constant frequency of 100 Hz was used for all experiments as we did not observe any frequency dependence during electric field alignment at a constant voltage.

At low voltages, the birefringence rise was slow and eventually reached a plateau value at relatively low levels (**Figure 3**). As the voltage was increased, the rate of rise of birefringence and final plateau value rapidly increased. Needless to say, viscosity plays a very important role in the reorientation kinetics. For the particles to rotate and orient, the torque due to dielectrophoretic force which is directly proportional to induced dipole and applied voltage has to be greater than the inertial and drag forces contributed by the viscosity. Interparticle interactions allows the sytem to reach a quasi-equilibrium (plateau) state as a critical amout of electric field is required to break that interaction. The viscosity increases with the increase in clay concentration (Figure S2, Supporting Information), along with the interparticle interactions. At higher concentration of clays, the size of tactoids were much larger compared to low concentrations as exfoliation becomes more difficult. When the three different concentrations of clay were compared at a single voltage, both the rate of orientation and final orientation decreased with increasing clay concentration (Figure 3d).

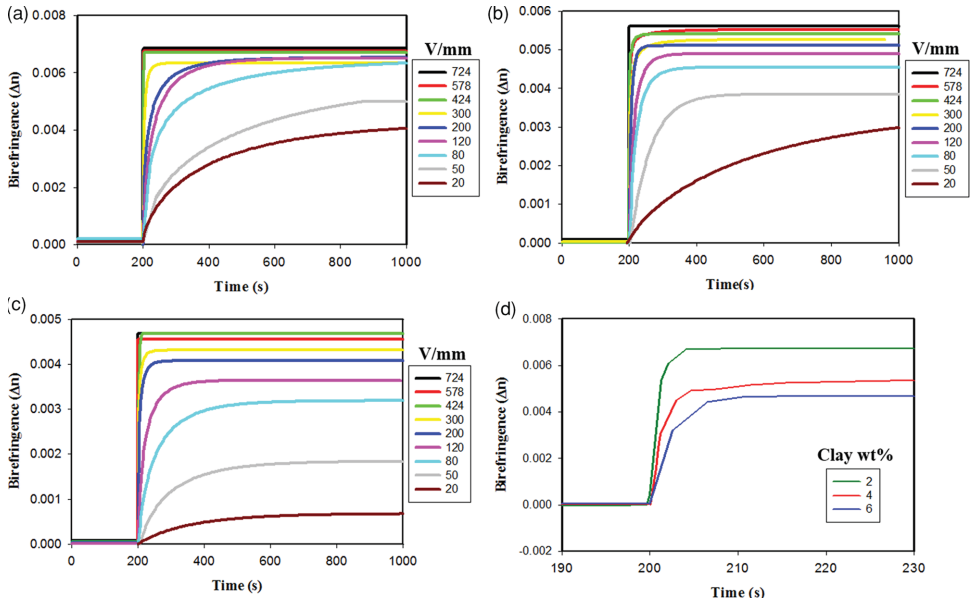

Figure 3. Kinetics of clay orientation as detected by birefringence response at a series of voltages and clay concentrations of a) 2 wt%, b) 4 wt%, and c) 6 wt%, and d) birefringence response to varying clay concentrations at fixed voltage of 120 V/mm.

To further elucidate and study the effect of voltage on the alignment of clay platelets at varying concentrations, the electro-optic behavior was expressed using Equation 3 which helps to correlate the birefringence values with the voltage and exposure time:

$$\frac{\Delta n^V(t) - \Delta n_0^V}{\Delta n_f^V - \Delta n_0^V} = 1 - \exp\left(-\frac{t}{av}\right) \quad (3)$$

where, $\Delta n^V(t)$ is the birefringence at any time t, Δn_0^V is the initial birefringence, Δn_f^V is the final birefringence, and a_V is the characteristic time for the applied voltage V.

Equation 3 can be used to fit the non-linear response of the clay during alignment under electric field. It can also be used to predict Δn values for all voltages and concentrations of clays which implies the electric field strength and duration time are complementary. Therefore, normalized birefringence was plotted as a function of reduced time, t/a_V, to obtain a master curve (**Figure 4**a) that is independent of the applied field. This was plotted for all three different clay loadings (Figure S3, Supporting Information), which, in turn, implies a universal relationship between the electric field strength and time of exposure during the structural development. Equation 3 used is similar to the time temperature superposition, hence it is called the electro-optic superposition principle (EOSP) relating exposure time and electric field strength with orientation.[64]

Using the EOSP, shift factors were obtained at different voltages. When the shift factors were plotted against the applied voltage, a non-linear response was observed. This was attributed to the fact that above a saturation voltage, there was little or no change in the birefringence and the rate at which the birefringence value was achieved, but at lower clay concentrations the saturation voltage was much lower compared to samples with higher clay loading. As indicated earlier, this is because of the increase in viscosity with higher loading and also increase in frustration between the particles due to interparticle interaction during electric field alignment. However, the linear response of the shift factor, which was similar at all three concentrations of clay loading, indicated that the shift factor has an exponent of −1.5 (Figure 4b). Hence, the EOSP can be used to tailor the alignment of anisotropic particles under electric field by selecting the voltage and time for desired orientation.

Polarized light microscopy is useful in assessing the orientation of individual particles when they exhibit inherent anisotropy. Optical micrographs (**Figure 5**a) were taken with first order red tint lambda (λ) plate (553 nm, red wave plate) inserted with the gamma direction (highest refractive index direction indicated in Figure 5a) at 45° to the crossed polarizer and analyzer. The particles oriented with higher refractive index axis parallel to the gamma direction (slow axis) appeared

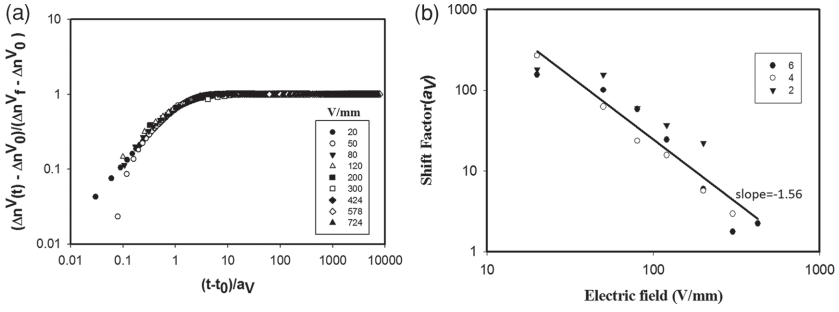

Figure 4. a) Master curves from normalized birefringence and reduced time developed using electro-optic superposition principle (EOSP) for 6 wt% clay loading and b) dependence of shift factor on electric field strength.

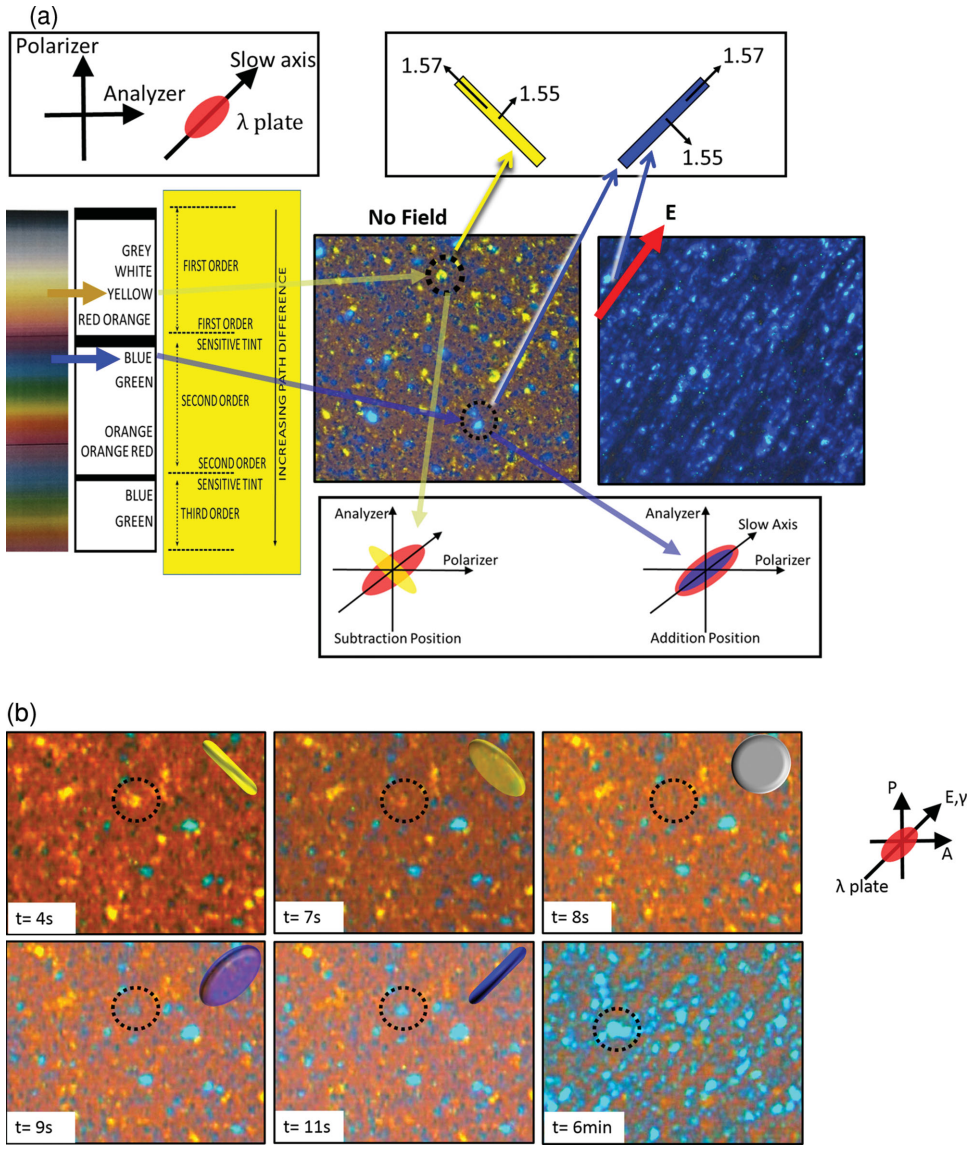

Figure 5. a) Birefringence response of clay platelets aligned under electric field observed with polarized optical microscope with first order red wave plate b) time sequence images showing rotation of particles in the electric field (40 V/mm) with the electric field parallel to the slow axis of red wave λ plate.

blue as they were in addition position with high refractive index direction of the particles oriented in the same direction as the high refractive index direction of the (λ plate and particles with higher refractive index normal to the gamma direction appeared yellow as they were in subtraction position.

The clay platelets aligned in-plane were observed under the polarized optical microscope with a red wave plate. When a randomly oriented monomer mixture of clay platelets was placed under the cross polarizers and the red wave plate, all observable colors including yellow and blue color platelets were seen as they were oriented in different directions due to randomness of the mixture. With the application of electric field normal to the slow axis of the red wave plate all particles turned yellow; similarly when electric field direction was parallel to the slow axis, they turned blue. As discussed earlier, clay platelets exhibit higher refractive index (1.57) in the basal plane when compared to the normal to the plane (1.55). Therefore, with the application of electric field all platelets changed to the same color under the red wave plate showing that the major axis or the higher refractive index axis was oriented in the direction of the electric field. However, it is important to note that since the refractive index of the clay platelets within the basal plane was the same in all directions, clay particles with this orientation appeared red.

When the electric field (V = 40V/mm) application direction set parallel to the slow axis, the time sequence of images showed rotational motion of the highlighted clay platelet. The color of the particle changed from yellow (subtraction position) to blue (addition position) as it rotated with higher refractive index parallel to the electric field or parallel to the slow axis of the red wave plate (Figure 5b). As depicted by the schematic, the yellow particle first rotated to go to darker red state

at t = 8 s where Δn = 0, following this state it became blue (t = 11s) depicting the higher refractive index or major axis parallel to the red wave plate. With increasing voltage, the color transition occurs faster showing faster orientation of particles. Above a critical voltage, all the particles turned blue instantaneously upon the application of the electric field oriented parallel to the slow axis. The video in the Supporting Information shows the real time transition of particles from randomly oriented state to aligned state where higher refractive index of the clay platelets align in the direction of the electric field.

Dielectrophoresis additionally causes both rotational and translational motion due to non-uniform field. An important manifestation of dielectrophoresis is dipole-dipole interaction that occurs even in a uniform electric field, a polarization field on one inclusion disturbs the electric field on the neighboring inclusion, hence producing attractive and repulsive forces between these inclusions. These attractive and repulsive forces lead to formation of chains of the inclusions in the matrix (**Figure 6**b). To observe the formation of chains and aligned orientation the morphology of the clay nanocomposites was studied using the optical and electron microscopes.

In TEM images (Figure 6a), only edges of the clay platelets were visible when observing the oriented film in the direction perpendicular to the electric field (top view).Examination of surface parallel to the electric field through SEM, revealed that the major axes of the clay are aligned parallel to electric field (Figure 6a).

SEM was also used to observe the chaining of the tactoids and single platelets by studying the surface parallel to the electric field direction. The SEM image shows the overall view of the cross section where the edges of the clay platelets were chained in the direction of the electric field, some of the chains are marked for ease of observation (Figure 6b). To further illustrate the chaining, we recorded a video under the polarized microscope shown in the supplemental information. The orientation of clay platelets was random in the plane, the (001) plane normals are oriented randomly transverse to electric field.

The induced orientational order parameter can be calculated from the birefringence values using

$$\%\text{orientation} = \left(\frac{\Delta n - \Delta n_0}{\dot{\Delta}}\right) \times 100 \tag{4}$$

where, $\dot{\Delta}$ = 0.01 intrinsic birefringence of the clay platelets (**Figure 7**a inset) as the matrix resin does not contribute to the measured orientation as mentioned earlier.

With the increase in clay loading, the level of orientation decreased (Figure 3). With 2 wt% clay loading, the orientation of clay platelets through the thickness of the film was around 70–75% (Figure 7a), however, at higher clay loadings of 6 wt% the orientation decreased to 50%. This is attributed to the increase in frustration between the particles due to interparticle interaction as shown in the schematic (Figure 7a inset). The saturation voltage was also observed by plotting orientation factor with the square of voltage (Figure S4, Supporting Information). No change in orientation occurred above this critical voltage.

The rate at which the orientation occurred was calculated from the slope of the birefringence vs voltage curves (Figure 3). A sigmoidal behavior was observed for the rate of change of orientation when plotted against voltage (Figure 7b). The dielectrophoretic force competed against inertia and drag forces as shown in the schematic (Figure 7b, inset). Hence, at lower voltages only single platelets and smaller tactoids rotated, whereas with increase in voltage, the dielectrophoretic force increased overcoming the inertial and drag forces and giving a higher rate of orientation. Increase in particle concentration increased inertial and drag forces, due to the increase in viscosity and

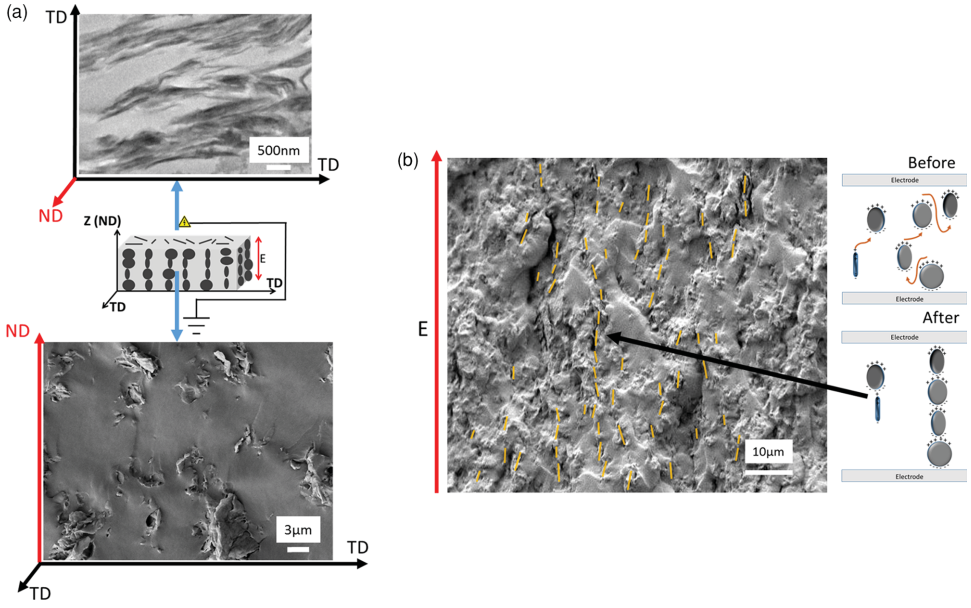

Figure 6. a) Orientation of clay was observed by TEM of microtomed samples microtomed through surface showing in-plane and fractured cross section SEM images showing out-of-plane orientation. b) Chaining of clay platelets observed through cross section SEM with visible clay edges marked with yellow lines and schematic of the dielectrophoretic chaining.

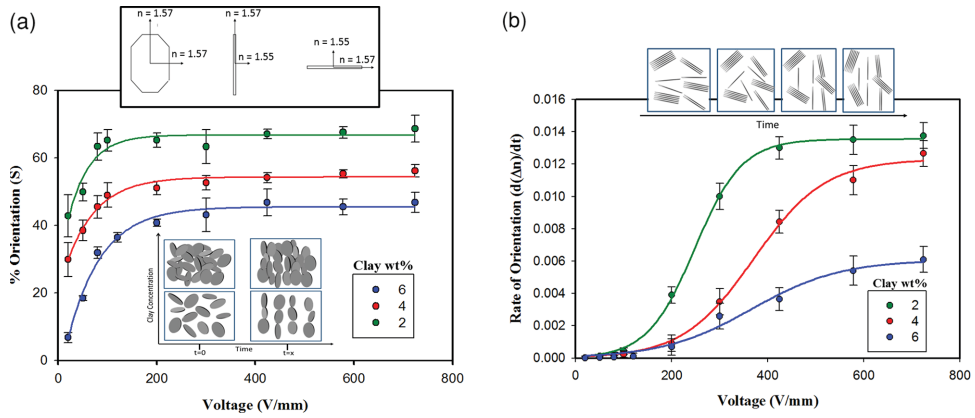

Figure 7. a) Effect of voltage on change in orientation calculated through birefringence (inset showing schematic showing movement of clay platelets with change in clay concentration) and b) kinetics of orientation of clay platelets at different voltages and concentrations (inset showing schematic of movement of single platelet and tactoids in electric field, at a constant viscosity the single platelets/smaller tactoids were easy to rotate)

interparticle interaction. Therefore, the rate of orientation decreased considerably with increase in particle concentration.

$$S = \frac{1}{2}\left\langle 3\cos^2\theta - 1 \right\rangle \quad (5)$$

2.3. XRD of Aligned Nanocomposites

The samples were further characterized off-line using WAXS diffraction patterns for clay orientation. The (001) Bragg diffraction ring from crystal lattice of the still intact layered clay platelets (Cloisite 30B) is located at 18.5 Å. Three X-ray patterns were obtained with X-rays directed along two mutually perpendicular transverse directions (TD) and one out of plane normal direction (ND). With applied voltage, we observed that the clay platelets orient in the Z-direction or the thickness direction of the film, which is parallel to the applied electric field. However, there was no anisotropy and hence orientation observed when the X-rays pass through the thickness of the film were in agreement with the zero in-plane birefringence observations earlier (**Figure 8**a). Also, as the voltage increased, the azimuthal breadth of diffraction peak became narrower signifying increase in preferential orientation of these particles. The orientation parameters were further calculated by plotting the intensity as a function of the azimuthal angle, the orientation factor was given by

where, S is the orientational order parameter and θ is the angle between the clay platelet and the normal director. For a perfectly oriented system $S = -0.5$. The order parameter decreased with increasing voltage. As the clay orientation increased, the order parameter at low clay loadings and high voltages was $S = -0.4$ which is very close the theoretical limit of –0.5.

Orientation factors calculated (Figure 8b) from birefringence measurements and X-ray diffraction were determined to be distinctly different. Birefringence technique provides ensemble average of orientation of particles regardless of their state of exfoliation and is very sensitive to rapid changes in optical anisotropy. WAXS relies on the presence of crystalline lattice, meaning multiple layered tactoids and intercalated clay structures to show diffraction peak. Hence, the WAXS technique does not sample fully exfoliated platelets and is blind to their reorientation behavior. Since the large particles (tactoids and intercalated particles) reorient slower in a given field due to the drag forces, they exhibit lower orientation as detected by WAXS.

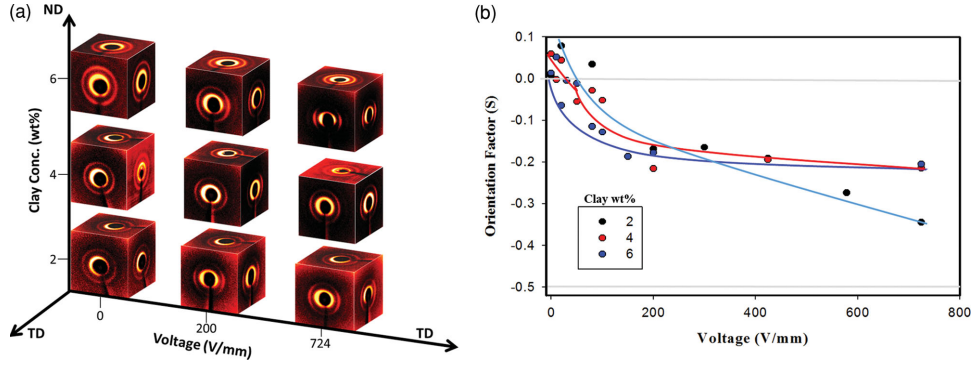

Figure 8. a) WAXD patterns taken with X-rays taken in three principal directions and b) orientation factors calculated from XRD for different voltages and concentration.

2.4. Roll-to-Roll Electric Field Assisted Alignment

To the best of our knowledge, a Roll-to-Roll manufacturing process for electric field assisted alignment to make Z-oriented functional films has not been demonstrated. The most common approaches for electric field alignment through the thickness are batch processes that include two electrodes separated by spacers, with the solution poured in between the electrodes and cured using thermal or UV curing after the application of electric field; however transparent electrodes are required for UV curable matrices. As has been previously studied, for electric field alignment to be effective, it is necessary to have the two electrodes touching the solution. If the electrodes are separated by an air gap the undulation occurs on the top of the polymer film, since the solution as a whole is polarized and attracted towards the electrode.[65,66]

Continuous electric field alignment of clay particles dispersed in photocurable resin as the matrix was carried out. The electric field setup is part of a newly developed large roll-to-roll manufacturing machine called electromagnetic processing (EMP) line, detailed elsewhere,[57,67] and is capable of applying three electric, magnetic and thermal gradient fields depending on the specifics of the materials to be oriented.

The electric field setup consists (**Figure 9**a) of two PVC rollers that are connected to a back plate that in turn sits on two rails connected to pneumatic motor used to jog the whole assembly upwards and downwards (Z-direction), thereby controlling the distance between the rollers and the steel belt or any conducting substrate acting as ground. A continuous loop of transparent ITO coated PET film surrounds these rollers and it is pre-tensioned using the spring loaded assembly on one of the rollers. This ensemble acts as the top electrode. The rollers are also connected to a drive motor allowing a forward and backward motion of the ITO coated PET at different speeds. In most cases the speed of the ITO coated PET film on top of the rollers is matched with the speed of the stainless steel belt below. This is done to prevent any shearing effect on the cast film. After adjusting the speed, the whole assembly is lowered to match the distance between the PET film and the substrate to that of the thickness of the cast films. A copper roller is placed on top of the PET film, this copper roller is connected to a high voltage power supply. The HV amplifier (Matsuda, model 20B20) can be used to generate a DC voltage, this amplifier is combined with an H-P function generator and can generate three types of fields: AC, DC, and biased AC fields. The copper roller is spring loaded and hence is always in contact with the conducting film while rotating with the film as it moves, creating a potential difference between the ITO coated PET film on top and the substrate. A UV wand that radiates at the wavelength suitable for curing the resin to freeze the aligned morphology is placed in the center of the setup.

During a typical process, particles are first dispersed in the photocurable resin using sonication, magnetic stirring, high shear mixing or other dispersion techniques. The monomer mixture is then cast onto the carrier using a slot die or a doctor blade assembly. The blade gap is set using the micrometers or feeler gauges to the desired thickness of the films. The gap between the top electrode film (ITO coated PET film) and the conducting substrate is kept smaller than the thickness of the cast film. The speed of the substrate and the top ITO coated film is then matched. As the cast film approaches the electric field setup it touches the transparent conducting film on top, while the top electrode is maintained at high voltage using a copper contact roller. After the sample orients due to the potential difference between the two electrodes, it is necessary to freeze the structure before the film reaches the end of the setup. This is carried out by irradiating UV light uniformly through the width of the sample using a UV wand, curing the cast film. Surface energy of the substrate is always kept higher than that of the transparent top electrode. This helps the film to always peel off from the top electrode making the film stick to the bottom substrate. During the rewinding of the films, these oriented films can first be peeled off and rewound separately or can be wound with the substrate.

To establish that the electric field induced alignment can be accomplished using the roll-to-roll setup with realistic manufacturing conditions, we were able to cast films of oriented clay (3" wide and 10" long) nanocomposites at 2, 4, and 6 wt% clay concentration with applied voltage of 724 V/mm at 10 cm/min speed. To verify the uniformity of orientation of the samples, WAXS patterns were obtained at different positions in the sample. The aligned 6 wt% clay nanocomposite had the

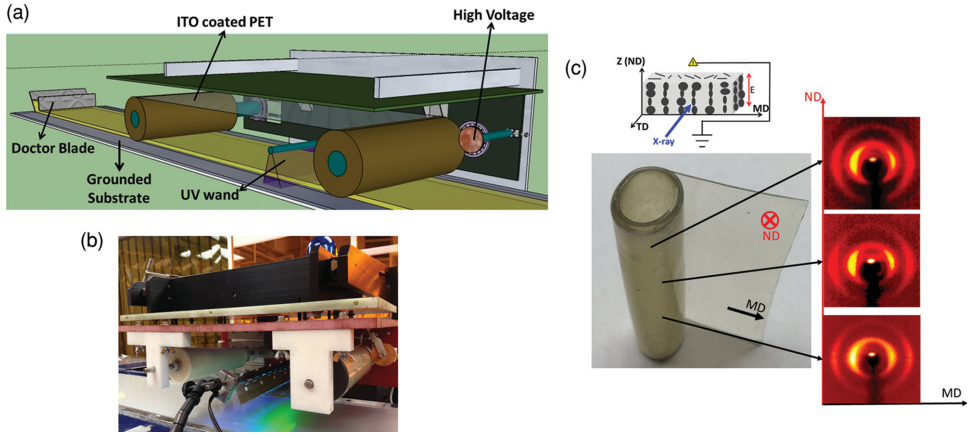

Figure 9. a) Schematic and b) picture of roll-to-roll processing equipment developed to create indefinitely long oriented films using electric field alignment. c) WAXS patterns at different locations for a roll of film with 6 wt% clay loading aligned at 724 V/mm.

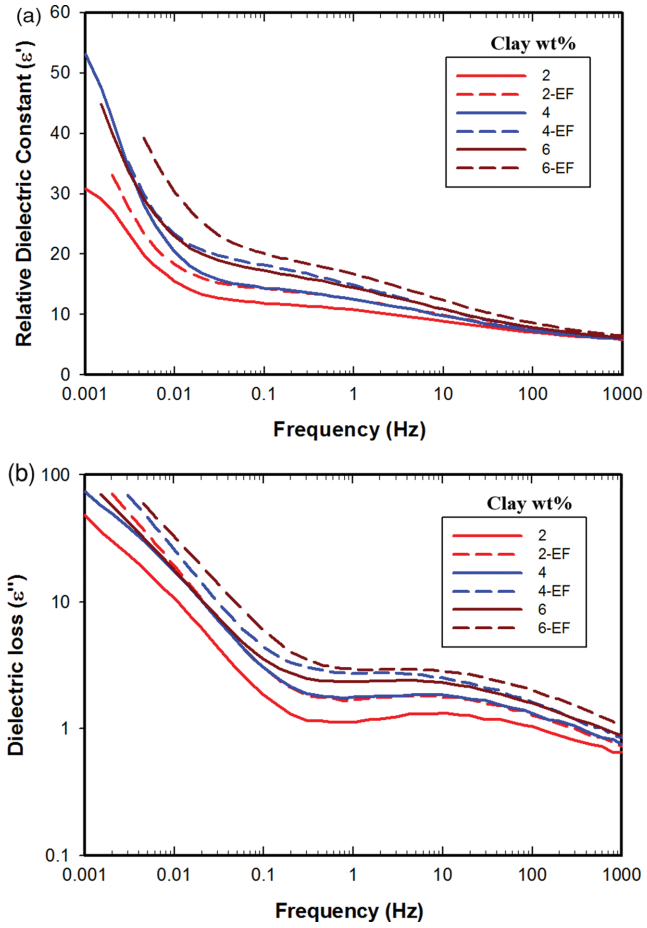

Figure 10. Enhancement of dielectric properties electric field oriented clay filled nanocomposites a) relative dielectric constant and b) dielectric loses (EF: Aligned nanocomposite film).

orientation factor S of –0.2 ± 0.02. Figure 9c shows the flexible oriented clay nanocomposite film and WAXS patterns at three locations of the film.

2.5. Ionic Conductivity Enhancement in Aligned Nanocomposites

Finally, we demonstrate the enhancement in *Z*-direction properties of clay nanocomposites using dielectric measurements on the roll-to-roll processed oriented films. The dielectric properties of both oriented and unoriented films at a series of clay concentration were measured through the thickness of the film. **Figure 10** compares the dielectric permittivity and dielectric loss of unoriented and oriented samples at room temperature. The dielectric constant above 100 Hz does not show any variation in between the oriented and unoriented clay nanocomposites due to the lack of dipole orientation. The dielectric constant starts increasing below 100 Hz to 0.03 Hz for filled systems as compared to unfilled systems as the clay filled nanocomposites incorporate more ionic dipoles leading to ionic polarization. The dielectric properties of oriented clay nanocomposites in this region is further enhanced due to the formation of oriented ionic dipoles. As we go below the frequency of 0.03 Hz there is an drastic increase in dielectric constant with increasing clay concentration due to charge migration at the electrode-polymer interface leading to electrode polarization.[38] The increase in dielectric properties below 0.03 Hz is attributed to ionic conductivity of clay platelets. Electrode polarization also causes an increase in the dielectric loss, this loss dominates the true dielectric loss from the clay nanocomposites till 1Hz.

Clay nanocomposites have anisotropic ionic conductivity in parallel and perpendicular oriented films.[68] It has been suggested that the difference in ionic conductivity of MMT nanocomposites is due to tortuosity of ionic migration which is caused by the orientation direction of MMT layers perpendicular to the measurement direction.[69] Therefore, MMT nanocomposites show higher ionic conductivity if the MMT layers are oriented in the direction of measurement compared to perpendicular orientation.[70] Below 0.03 Hz, oriented samples show much higher dielectric constant as compared to the unoriented samples. This is attributed to the fact that the oriented nanocomposites have higher ionic conductivity since the ionic migration is much easier when clays are oriented parallel to the direction of measurement. Also, the oriented nanocomposites have higher interparticle interaction due to chaining of clay platelets caused by dielectrophoretic alignment, making the ionic migration easier leading to the higher dielectric constant for the oriented samples. Hence, *Z*-oriented clay nanocomposites can be used to increase the ionic conductivity at lower particle concentrations.

3. Conclusions

The electric field assisted alignment allows *Z*-(thickness direction) alignment and organization of nanoparticles facilitating the tailoring of properties in this direction. These include thermal conductivity, dielectric properties, barrier properties, ion exchange depending on the filler. In this study, the development of birefringence measurement system was described coupled with electric field. Using this tool, kinetics of *Z*-direction orientation in the presence of electric field was studied. This information enabled the development of electro-optic superposition principle that relates the birefringence, voltage and time. As a result, the properties of nanocomposites can be tailored by selecting required voltage and time to obtain required microstructures. The orientation of the clay particles substantially enhanced the ionic conductivity properties in oriented nanocomposites. A roll-to-roll process to obtain *Z*-oriented nanocomposites has also been reported for the first time. This is critical for commercializing oriented polymer nanocomposites with *Z*-enhanced properties.

4. Experimental Section

Prepartion of Nanocomposites: Clay nanocomposites were prepared using Cloisite 30B (organo-modified clay from southern clay products) as the filler and a photocurable resin Norland 65 (Norland products) as the matrix. Both the matrix and the filler were used as is without any further modifications. The photocurable resin NOA65 was chosen

since it is a colorless, clear liquid photopolymer, thus making the birefringence measurements possible at different wavelengths. It is reported in literature that this compound is made essentially of four constituents: trimethylolpropane diallyl ether, trimethylolpropane tris thiol, isophorome di-isocyanate ester and 5 wt% photoinitiator benzophenone. NOA65 cures when exposed to ultraviolet light and has fast curing times with maximum absorption between 350–380 nm at ambient temperatures. This eliminates the heat curing and post curing operation common in other adhesives. The fast curing helps to freeze the structure rapidly at required morphology and leads to faster production time during the roll-to-roll process, since the polymer curing is the time determining step when compared to the alignment step which typically takes a few seconds. The curing by UV light generates radicals that start a chain of polymerization reactions according to the standard process. Being a one part system containing 100% solids, the shrinking effects upon curing are minimized and therefore the gap between the two electrodes during the alignment can be kept constant. The cured adhesive is flexible and transparent even at higher clay loadings. The clay particles were dispersed in the resin using Hielscher UP400S ultrasonic processor and planetary centrifugal mixer (Thinky Mixer) to achieve reproducible dispersion for all samples. The suspensions were then loaded between two ITO coated transparent glasses obtained from SPI supplies with 1mm glass spacers. Different voltages at varying frequencies were applied between the two conducting ITO electrodes and the retardation was measured real time using the equipment described earlier. The morphology after applied electric field was frozen by shining UV light on top of ITO coated glass using OmniCure 2000 UV lamp.

Sample Characterization: The morphology of cured films was characterized using X-ray diffraction, transmission electron microscope (JOEL-1230) and scanning electron microscope (JEOL JSM 5310). Bruker AXS Generator equipped with a copper tube and a two dimensional detector was used to obtain the XRD patterns of the oriented films. The generator was operated at 40 kV and 40 mA with a beam monochromatized to Cu Kα radiation. A typical exposure time of 20 min was used. The optical microscope used to study the orientation was a Leitz Laborlux 12 Pol S microscope stage between the crossed polarizers. A first order red wave plate was also inserted with its slow axis oriented at 45° to the crossed polarizers. The pictures of the samples were taken with a DC 290 Kodak Zoom digital camera connected to the optical microscope.

Supporting Information

Supporting Information is available from the Wiley Online Library or from the author.

Acknowledgements

The authors gratefully acknowledge the funding from Third Frontier, Wright Center of Innovation program (CMPND) of The State of Ohio. The authors would like to thank JoAnne Ronzello from University of Connecticut for dielectric spectroscopy measurements.

Received: March 7, 2014
Revised: August 28, 2014
Published online: October 6, 2014

[1] D. R. Paul, L. M. Robeson, *Polymer* **2008**, *49*, 3187.
[2] L. Arboleda, A. Ares, M. J. Abad, A. Ferreira, P. Costa, S. Lanceros-Mendez, *J. Polym. Res.* **2013**, *20*, 326.
[3] M. Ibáñez, R. Zamani, S. Gorsse, J. Fan, S. Ortega, D. Cadavid, J. R. Morante, J. Arbiol, A. Cabot, *ACS Nano* **2013**, *7*, 2573.
[4] J. R. Potts, D. R. Dreyer, C. W. Bielawski, R. S. Ruoff, *Polymer* **2011**, *52*, 5.
[5] A. J. Crosby, J. Lee, *Polym. Rev.* **2007**, *47*, 217.
[6] S. C. Tjong, *Mater. Sci. Eng. R Rep.* **2006**, *53*, 73.
[7] Z. Guo, T. Pereira, O. Choi, Y. Wang, H. T. Hahn, *J. Mater. Chem.* **2006**, *16*, 2800.
[8] C. Lu, Y.-W. Mai, *Phys. Rev. Lett.* **2005**, *95*, 088303.
[9] B. Xu, Q. Zheng, Y. Song, Y. Shangguan, *Polymer.* **2006**, *47*, 2904.
[10] M. Tanimoto, T. Yamagata, K. Miyata, S. Ando, *ACS Appl. Mater. Interfaces* **2013**, *5*, 4374.
[11] T. Lai, M. Mortland, *Clays Clay Miner.* **1968**, *16*, 129.
[12] R. Basu, G. S. Iannacchione, *Appl. Phys. Lett.* **2009**, *95*, 173113.
[13] A. L. González, C. Noguez, A. S. Barnard, *J. Mater. Chem. C* **2013**, *1*, 3150.
[14] V. V. Ganesh, N. Chawla, *Mater. Sci. Eng. A* **2005**, *391*, 342.
[15] Y. Konishi, M. Cakmak, *Polymer* **2005**, *46*, 4811.
[16] B. Yalcin, M. Cakmak, *Polymer* **2004**, *45*, 2691.
[17] D. A. Kunz, J. Schmid, P. Feicht, J. Erath, A. Fery, J. Breu, *ACS Nano* **2013**, *7*, 4275.
[18] A. M. Marconnet, N. Yamamoto, M. A. Panzer, B. L. Wardle, K. E. Goodson, *ACS Nano* **2011**, *5*, 4818.
[19] B. R. Vaughan, E. Marand, *J. Memb. Sci.* **2008**, *310*, 197.
[20] H. Lin, L. Li, J. Ren, Z. Cai, L. Qiu, Z. Yang, H. Peng, *Sci. Rep.* **2013**, *3*, 1353.
[21] Y. Zhang, Y. Wang, Y. Deng, Y. Guo, W. Bi, M. Li, Y. Luo, J. Bai, *Appl. Phys. Lett.* **2012**, *101*, 192904.
[22] D. Yuan, Z. Liu, S. W. Tay, X. Fan, X. Zhang, C. He, *Chem. Commun.* **2013**, *49*, 9639.
[23] W. Huynh, J. Dittmer, N. Teclemariam, D. Milliron, A. Alivisatos, K. Barnham, *Phys. Rev. B* **2003**, *67*, 115326.
[24] K. D. Hermanson, S. O. Lumsdon, J. P. Williams, E. W. Kaler, O. D. Velev, *Science* **2001**, *294*, 1082.
[25] V. Olszowka, M. Hund, V. Kuntermann, S. Scherdel, L. Tsarkova, A. Böker, *ACS Nano* **2009**, *3*, 1091.
[26] E. S. Choi, J. S. Brooks, D. L. Eaton, M. S. Al-Haik, M. Y. Hussaini, H. Garmestani, D. Li, K. Dahmen, *J. Appl. Phys.* **2003**, *94*, 6034.
[27] T. Prasse, *Compos. Sci. Technol.* **2003**, *63*, 1835.
[28] G. Choudalakis, A. D. Gotsis, *Eur. Polym. J.* **2009**, *45*, 967.
[29] M. W. Möller, D. A. Kunz, T. Lunkenbein, S. Sommer, A. Nennemann, J. Breu, *Adv. Mater.* **2012**, *24*, 2142.
[30] M. M. Malwitz, S. Lin-Gibson, E. K. Hobbie, P. D. Butler, G. Schmidt, *J. Polym. Sci. Part B Polym. Phys.* **2003**, *41*, 3237.
[31] L. M. C. Dykes, J. M. Torkelson, W. R. Burghardt, *Macromolecules* **2012**, *45*, 1622.
[32] K. C. Cole, F. Perrin-Sarazin, G. Dorval-Douville, *Macromol. Symp.* **2005**, *230*, 1.
[33] B. Yalcin, M. Cakmak, *J. Polym. Sci. Part B Polym. Phys.* **2005**, *43*, 724.
[34] M. Okamoto, P. H. Nam, P. Maiti, T. Kotaka, T. Nakayama, M. Takada, M. Ohshima, A. Usuki, N. Hasegawa, H. Okamoto, *Nano Lett.* **2001**, *1*, 503.
[35] H. Zhou, S. Zhang, M. Yang, *J. Appl. Polym. Sci.* **2008**, *108*, 3822.
[36] R. Prasanth, N. Shubha, H. H. Hng, M. Srinivasan, *Eur. Polym. J.* **2013**, *49*, 307.
[37] A. Guevara-Morales, A. C. Taylor, *J. Mater. Sci.* **2013**, *49*, 1574.
[38] E. David, M. Fréchette, B. Zazoum, C. Daran-Daneau, A. D. Ngô, H. Couderc, *J. Nanomater.* **2013**, *2013*, 1.
[39] K. Murata, K. Haraguchi, *J. Mater. Chem.* **2007**, *17*, 3385.
[40] N. Bitinis, M. Hernandez, R. Verdejo, J. M. Kenny, M. A. Lopez-Manchado, *Adv. Mater.* **2011**, *23*, 5229.
[41] E. Schaffer, T. Thurn-Albrecht, T. Russell, U. Steiner, *Nature* **2000**, *403*, 874.
[42] K. M. Ryan, A. Mastroianni, K. A. Stancil, H. Liu, A. P. Alivisatos , *Nano Lett.* **2006**, *6*, 1479.

[43] M. Knaapila, J. P. Pinheiro, M. Buchanan, A. T. Skjeltorp, G. Helgesen, *Carbon* **2011**, *49*, 3171.
[44] T. C. Halsey, *Science* **1992**, *258*, 761.
[45] D. A. van denEnde, S. E. van Kempen, X. Wu, W. A. Groen, C. A. Randall, S. van der Zwaag, *J. Appl. Phys.* **2012**, *111*, 124107.
[46] G. Kim, Y. M. Shkel, *J. Mater. Res.* **2004**, *19*, 1164.
[47] A. Ramos, H. Morgan, N. G. Green, A. Castellanos, *J. Phys. D. Appl. Phys.* **1998**, *31*, 2338.
[48] B. Huang, T. G. M. van de Ven, R. J. Hill, *J. Phys. Chem. C* **2011**, *115*, 8447.
[49] R. a. Rica, M. L. Jiménez, Á. V. Delgado, *Soft Matter* **2012**, *8*, 3596.
[50] H. Koerner, J. D. Jacobs, D. W. Tomlin, J. D. Busbee, R. A. Vaia, *Adv. Mater.* **2004**, *16*, 297.
[51] Z. Rozynek, T. Zacher, M. Janek, M. Čaplovičová, J. O. Fossum, *Appl. Clay Sci.* **2013**, *77–78*, 1.
[52] Z. Rozynek, K. D. Knudsen, J. O. Fossum, Y. Méheust, B. Wang, M. Zhou, *J. Phys. Condens. Matter* **2010**, *22*, 324104.
[53] I. Dozov, E. Paineau, P. Davidson, K. Antonova, C. Baravian, I. Bihannic, L. J. Michot, *J. Phys. Chem. B* **2011**, *115*, 7751.
[54] A. Bakk, J. Fossum, G. da Silva, H. Adland, A. Mikkelsen, A. Elgsaeter, *Phys. Rev. E* **2002**, *65*, 021407.
[55] M. L. Jiménez, L. Fornasari, F. Mantegazza, M. C. D. Mourad, T. Bellini, *Langmuir* **2012**, *28*, 251.
[56] E. Unsal, J. Drum, O. Yucel, I. I. Nugay, B. Yalcin, M. Cakmak, *Rev. Sci. Instrum.* **2012**, *83*, 025114.
[57] M. Cakmak, *WO Pat. WO/2011/008,870,* **2011**.
[58] O. Yucel, E. Unsal, M. Cakmak, *Macromolecules* **2013**, *46*, 7112.
[59] Y. Eguchi, E. Unsal, M. Cakmak, *Macromolecules* **2013**, *46*, 7488.
[60] E. Unsal, M. Cakmak, *Macromolecules* **2013**, *46*, 8616.
[61] C. I. Martins, M. Cakmak, *Polymer* **2007**, *48*, 2109.
[62] R. S. Stein, *J. Polym. Sci.* **1957**, *24*, 383.
[63] C. Park, R. E. Robertson, *Mater. Sci. Eng. A* **1998**, *257*, 295.
[64] J. U. Park, Y. S. Choi, K. S. Cho, D. H. Kim, K. H. Ahn, S. J. Lee, *Polymer* **2006**, *47*, 5145.
[65] G. Amarandei, P. Beltrame, I. Clancy, C. O'Dwyer, A. Arshak, U. Steiner, D. Corcoran, U. Thiele, *Soft Matter* **2012**, *8*, 6333.
[66] R. Verma, A. Sharma, K. Kargupta, J. Bhaumik, *Langmuir* **2005**, *21*, 3710.
[67] M. Cakmak, S. Batra, B. Yalcin, *Polym. Eng. Sci.* **2014**.
[68] P. Aranda, E. Ruiz-Hitzky, *Chem. Mater.* **1992**, *4*, 1395.
[69] J. C. Hutchison, R. Bissessur, D. F. Shriver, *Chem. Mater.* **1996**, *8*, 1597.
[70] S. Kitajima, M. Matsuda, M. Yamato, Y. Tominaga, *Polym. J.* **2012**, *45*, 738.